



## Design optimization of heat exchanger using deep reinforcement learning

Geunhyeong Lee<sup>a,\*</sup>, Younghwan Joo<sup>b</sup>, Sung-Uk Lee<sup>a</sup>, Taejoon Kim<sup>c</sup>, Yonggyun Yu<sup>a</sup>, Hyun-Gil Kim<sup>a</sup>

<sup>a</sup> Korea Atomic Energy Research Institute, 111, Daedeok-daero 989 beon-gil, Yuseong-gu, Daejeon 34057, Republic of Korea

<sup>b</sup> Korea Institute of Energy Research, 152, Gajeong-ro, Yuseong-gu, Daejeon 34129, Republic of Korea

<sup>c</sup> Mirae Engineering, B-316, 17 Techno 4-ro, Yuseong-gu, Daejeon 34013, Republic of Korea

### ARTICLE INFO

#### Keywords:

Heat exchanger  
Topology optimization  
Reinforcement learning  
3D printing  
Micro nuclear reactor  
PCHE

### ABSTRACT

A micronuclear reactor is currently being developed using 3D printing technology, with a focus on refining the design of its heat exchanger. The objective is to optimize the topology of heat exchangers to improve their performance. The initial thermofluidic topology design is a crucial factor influencing the efficiency of the final optimized heat exchanger. This paper presents a novel approach for the topology optimization of heat exchangers using initial designs generated via deep reinforcement learning (DRL). A printed circuit heat exchanger (PCHE) served as the target for this optimization. Extensive simulations demonstrated that the DRL-assisted optimization method enhanced the heat exchange efficiency by 14.8% compared with that of conventional topology-optimized PCHEs. The optimized heat exchanger was fabricated using 3D printing, and its feasibility was confirmed by comparison with simulation data. The integration of DRL into the topology optimization and production processes via 3D printing lays the groundwork for the development of more efficient thermal systems and demonstrates a viable method for complex engineering applications.

### 1. Introduction

In thermal engineering, the effective design and optimization of heat exchangers are crucial for enhancing energy efficiency in various applications. Topology optimization refers to the optimization of a heat exchanger configuration to realize the maximum heat exchange within a given space. Given their two-dimensional (2D) fluid flow geometries, printed circuit heat exchangers (PCHEs) are particularly suited to the complex demands of computational fluid dynamics and thermal topology optimization. This study focuses on the topology optimization of PCHEs, leveraging their advantageous design to realize intricate geometries and maximize thermal exchange efficiency using artificial intelligence.

PCHEs are widely used in diverse industries, including coal-fired power plants [1], molten-salt reactors [2], small modular reactors [3], sodium fast reactors [4], and solar tower power plants [5]. To maximize heat transfer, PCHEs can be equipped with various types of flow channels, such as zigzag, S-shaped, or airfoil fins [6,7]. However, determining the optimal PCHE configuration for each application is challenging, and the thermofluidic flow channel topology must be optimized to achieve maximum efficiency.

Several studies have contributed to the topology optimization of heat exchangers to enhance efficiency. Papazoglou [8] was the first to simulate a heat exchanger with separate flows, focusing on improving heat transfer between the two fluids. Saviers et al. [9] improved the three-dimensional (3D) design of this heat exchanger and successfully tested it for commercial use, showing that it was effective in reducing pressure loss in the flow while enhancing heat transfer. Høghøj et al. [10] applied a density-based design method to increase the thickness of the wall separating the two fluids in a heat exchanger. Feppon [11] and Feppon et al. [12] refined a heat exchanger design using the level-set method, which also ensured that the fluids did not mix. Lee et al. [13] focused on the topology optimization of PCHEs but noted the difficulty of substantially enhancing their heat exchange capabilities for industrial applications.

Thus far, the topology optimization of PCHEs has not achieved substantial enhancement of the heat exchange capability. Therefore, this study focused on increasing the heat exchanger performance by applying deep reinforcement learning (DRL) during the initial topology design, which considerably affects the performance of the final design [14]. Reinforcement learning can be applied to realize the generative design of a structure via topology optimization [15]. Jang et al. [16]

\* Corresponding author.

E-mail address: [leeg@frib.msu.edu](mailto:leeg@frib.msu.edu) (G. Lee).

used a data-driven topology optimization method comprising a generative design approach based on reinforcement learning to determine optimal design parameter combinations. Mekki et al. [17] combined a genetic algorithm-based topology optimization method with a computational fluid dynamics approach to generate organic heat exchanger fin designs. This study applied DRL to optimize the topology in the initial design phase so that the objective efficiency of the final heat exchanger design could be enhanced.

Topology-optimized designs can be complex, and their adaptation to real-world industrial applications can be challenging. Conventional manufacturing methods are often limited in terms of topology-optimized design structures. However, advancements in additive 3D printing manufacturing processes have expanded the possibilities for innovation in this field. Therefore, this study integrated DRL-assisted topology optimization with 3D printing to address many of the aforementioned challenges and provide a promising optimization approach for heat exchanger design and manufacturing.

## 2. Methods

### 2.1. Overall optimization procedure

This study targeted the PCHE shown in Fig. 1. This PCHE comprises stacked hot and cold plates, with heat exchanged between them. The proposed method is based on optimizing the flow path design of the hot and cold plates to maximize the heat exchange capacity.

The channel width in the targeted PCHE was 4 mm, the channel pitch was 2 times of each channel, and the water flow plate thickness was 2 mm. The plate was stacked with a 2 mm fluid flow plate and solid plate that separated each fluid plate. This design specification was determined to compare reinforcement learning design described in Section 2.3.

If the initial design for topology optimization provides sufficient heat exchange, the resulting topology-optimized design will provide high performance. However, determining an effective initial design for topology optimization in terms of heat exchange optimization is difficult. Therefore, DRL with proximal policy optimization (PPO) was applied to obtain an initial design for topology optimization [18]. The overall design process is illustrated in Fig. 2.

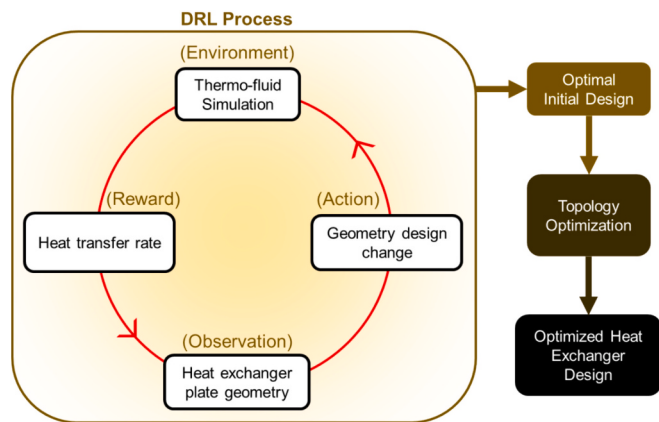


**Fig. 2.** General process of the proposed DRL-assisted topology optimization design method.

First, the heat and fluid solver were applied with DRL to interpret the heat exchange capability and determine the maximum reward, which is equivalent to the maximum heat exchange capability. Next, topology optimization was conducted on the DRL-assisted initial PCHE design by adjusting the initial design values. The results of topology optimizations undertaken with and without DRL-assisted initial designs were subsequently compared using 3D design simulations. Finally, the performance of the 3D-printed, DRL-assisted topology-optimized heat exchanger was compared with the simulation results for verification. The following sections provide detailed explanation for each method.

### 2.2. Topology optimization

Fig. 3 shows the standard design of a PCHE and illustrates how the three areas considered in the pseudo-3D optimization approach originated from the PCHE structure [19]. The PCHE was designed using alternating layers of hot and cold plates. Each plate was designed with fluid channels at specific locations for fluid entry and exit. As the hot and cold fluids pass through these channels during operation, heat flows from the hot fluid (the top design domain in Fig. 3) to the conduction

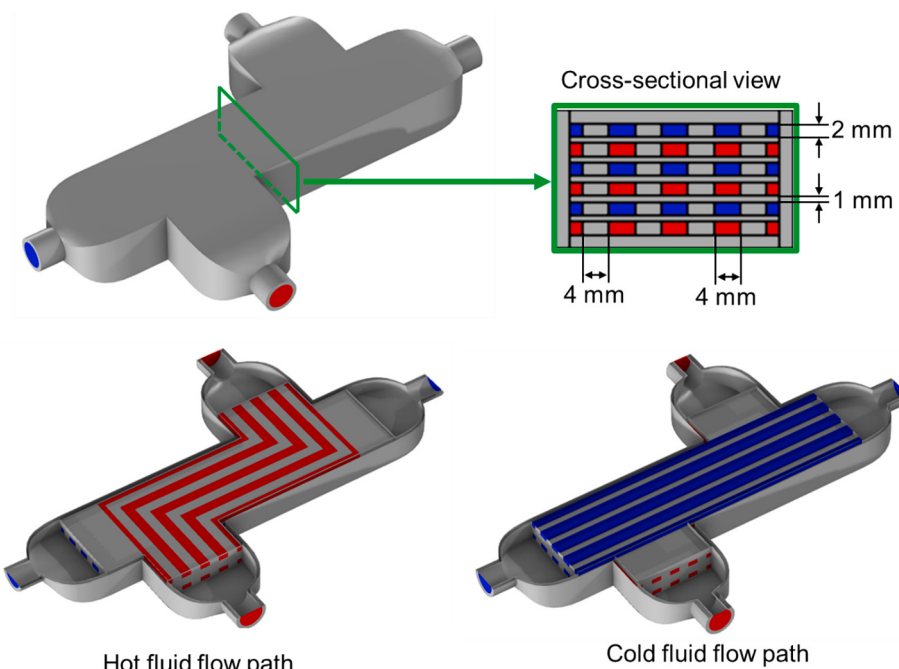


**Fig. 1.** General structure of the PCHE considered in this study.

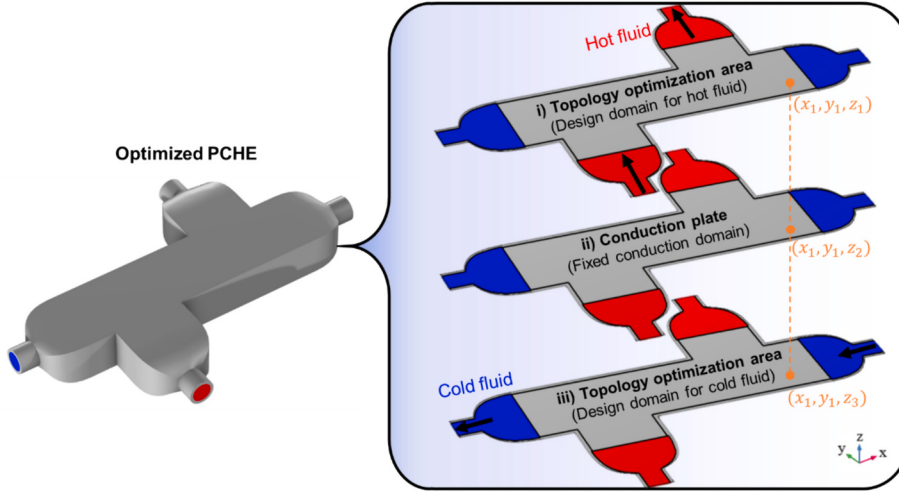


**Fig. 3.** Geometry of a conventional PCHE and heat transfer coupling design domains for the pseudo-three-dimensional method.

plate (the middle design domain in Fig. 3) situated between the hot and cold fluids. Subsequently, the heat travels from the conduction plate to the cold fluid (the bottom design domain in Fig. 3). Thus, two different 2D domains (the top and bottom in Fig. 3) were considered to optimize the PCHE design. For the hot- and cold-fluid domains, a location was considered solid or fluid depending on whether its density was 0 or 1, respectively. For the conduction plate, the input and output heat were considered identical; thus, the simulation for each plate could be performed iteratively.

In the hot and cold fluid design domains, a fully developed laminar flow was assumed with the Darcy term to apply the solid isotropic material with a penalization (SIMP) approach.

The governing equations for the thermofluidic simulation are as follows:

$$\rho(\mathbf{u} \bullet \nabla)\mathbf{u} = \nabla \bullet [-P\mathbf{I} + \mathbf{K}] - 12\frac{\mu\mathbf{u}}{d_z^2} - \alpha\mathbf{u} \quad (1)$$

$$\rho\nabla \bullet \mathbf{u} = 0 \quad (2)$$

$$d_z\rho C_p \mathbf{u} \bullet \nabla T - \nabla \bullet (d_z k \nabla T) = d_z Q_{\text{source}} \quad (3)$$

$\rho$ ,  $P$ ,  $u$ ,  $I$ ,  $K$ , and  $\mu$  represent the density, pressure, velocity, identity matrix, viscous stress tensor, and dynamic viscosity of the fluid, respectively.  $Q$  denotes the heat source,  $k$  is the thermal conductivity,  $C_p$  is the specific heat capacity, and  $T$  is the temperature. Moreover,  $\alpha$  and  $d_z$  denote the inverse permeability and channel thickness in the shallow channel approximation, respectively [20].

For the inverse permeability term  $\alpha$ , the Darcy penalization [21] ensures a high resistance to flow in the solid phase ( $\gamma = 0$ ) by setting  $\alpha_{\max}$  as a maximum value as follows:

$$\alpha = \alpha_{\max} \frac{q(1-\gamma)}{q+\gamma} \quad (4)$$

where  $q$  is the Darcy penalization factor. The higher inverse permeability interrupts the fluid flows by applying a force to the velocity fields ( $-\alpha \times u$ ), as expressed in Eq. (1).

The heat exchange between the two domains,  $Q_{\text{source}}$ , was calculated as follows:

$$Q_{\text{source}} = \begin{cases} \frac{h_{\text{hot}}}{d_z} (T_{\text{hot}} - T_{\text{plate}}) & \text{Hot fluid - Plate domain} \\ \frac{h_{\text{cold}}}{d_z} (T_{\text{cold}} - T_{\text{plate}}) & \text{Cold fluid - Plate domain} \end{cases} \quad (5)$$

where  $T_{\text{hot}}$ ,  $T_{\text{plate}}$ , and  $T_{\text{cold}}$  denote the temperatures of the hot, conduction-plate, and cold domains, respectively;  $h_{\text{hot}}$  and  $h_{\text{cold}}$  denote the heat-transfer coefficients of the hot and cold domains, respectively.

The interpolation function to determine the thermal conductivity of the grey area follows the application of the SIMP approach:

$$k(\gamma) = (k_s - k_f)\gamma^p + k_f \quad (6)$$

where  $k_s$  and  $k_f$  are the thermal conductivities of the solid and fluid, respectively;  $\gamma$  is the material density; and  $p$  is the penalty value.

Although no mass is transferred between the three domains, the heat transfer between them is closely coupled. As depicted in Fig. 3, the three domains share the same  $x$ - and  $y$ -positions, and they are aligned along the  $z$ -axis. Heat moves along the  $z$ -direction from the hot fluid through the conduction plate and into the cold fluid; thus, the same amount of  $Q_{\text{source}}$  was used in all three domains with negative and positive values for the heat exchanged between the hot- and cold-fluid domains, respectively, and the conduction plate. A constant inlet flow rate was assumed in both the hot and cold fluid domains, and the boundary conditions were as follows:

- Walls: (internal)  $\mathbf{u} = 0$ ; (external)  $\frac{\partial T}{\partial n} = 0$
- Cold fluid: (inlet)  $q' = q'_{\text{in}}, T = T_{\text{cold}}$ ; (outlet)  $P = 0$
- Hot fluid: (inlet)  $q' = q'_{\text{in}}, T = T_{\text{hot}}$ ; (outlet)  $P = 0$
- Topology boundary:  $\gamma_{\text{solid}} = 0, \Delta P \leq n \bullet P_{\text{initial}}$

where  $u$  denotes the velocity,  $q'$  represents the flow rate, and  $P$  denotes the pressure.

The optimization problem can be expressed as

$$\begin{aligned} \text{Maximize } Q_{\text{total}} &= \int_{\Omega_d} Q_{\text{source}} dV \\ \text{s.t. } \int_{\Omega_d} \gamma dV &\leq V_0 \\ \Delta P_{\text{hot}} &< P_{0,\text{hot}} \\ \Delta P_{\text{cold}} &< P_{0,\text{cold}} \end{aligned} \quad (7)$$

where  $Q_{\text{total}}$  represents the total heat exchange,  $V_0$  represents the average initial density of the material used in the PCHE design, and  $P_0$  indicates the designated limited pressure for avoiding abnormal condition flow path [13].

The globally convergent method of moving asymptotes was employed to identify the most efficient layout for the topology outcomes [22]. Constraints on the pressure drop within both the hot and cold fluid

domains were implemented to prevent excessive pressure drops that could potentially block the flow channel owing to the topology.

The design sensitivity expresses the variation in the objective gradient with alterations in topology. This gradient indicates whether the topology should be adjusted upward or downward to maximize the objective function. By considering the pressure boundary constraints in the sensitivity analysis, the optimal topology that enhanced the heat transfer efficiency was identified. The adjoint sensitivity method was chosen owing to its effectiveness in scenarios with many sensitivity parameters and fewer objective functions [23]. The overall corresponding optimization algorithm followed by Lee et al. [13].

In practical applications, minimizing the intermediate gray area is crucial, and to achieve this goal, a combination of a Helmholtz filter and tangent hyperbolic projection was employed [21]. The selection of the sweep parameter played a vital role in determining the optimal converged value. By iteratively adjusting the sweep parameter, the local minimum traps were effectively avoided, with the grey area reduced during the topology optimization process. Additionally, the penalty value ( $p$ ) was gradually increased from 2 to 4, and Darcy penalization values of 0.01, 0.1, and 0.1 were applied correspondingly to the sweep numbers from 1 to 3, respectively, shown in Table 1.

Furthermore,  $\alpha_{max}$  was empirically set to  $3 \times 10^6 \text{ Pa} \cdot \text{s/m}^2$  to reduce the gray area while enhancing the inverse permeability of the fluid. Finally, the ultimate optimized design was attained under a restricted boundary density condition of 0.7, ensuring that the 3D supporting section was preserved.

FEM simulations were conducted using the COMSOL 6.0. The size of the FEM mesh was established via empirical testing and set at 0.5 mm in a rectangular shape to strike a balance between computational efficiency and the accuracy of flow path optimization. The fluid was modeled as water and the solid material as 316 stainless steel with the specific properties listed in Table 2. To simplify the calculations and reduce computational demands, these properties were assumed to remain constant regardless of the temperature. The temperatures of the hot and cold fluids were fixed at 80 and 20 °C, respectively.

### 2.3. Obtaining an initial design using DRL

Determining the optimal initial topological shape of a heat exchanger can be difficult without extensive trial and error, and evaluating all potential design combinations requires considerable time. However, using DRL, an initial design for topology optimization can be determined promptly. Using pseudo-3D methods, the simulation condition was simplified to two 2D plates, namely cold and hot plates, to increase the calculation speed of DRL.

Fig. 4 shows the general design and DRL algorithm of the PCHE. The plate domain was separated into 80 cells, that is, 8 mm square cells. The objective of the DRL was to determine whether each cell was solid or fluid-like and to decide whether the cell size was 6 mm (for the solid) or 1 mm (for the fluid), considering the physical constraints of producing the actual heat exchanger using additive-manufactured metal 3D printing. The same model was used for the cold and hot plates to reduce computational cost. The proposed DRL approach combined the PPO algorithm with a convolutional neural network (CNN). The PPO, which is known for its proficiency in handling continuous action spaces, is crucial for the optimal control required in heat exchanger design; the CNN is essential for interpreting the complex spatial data inherent in the

**Table 1**  
Parameter sweep used in the simulation.

Parameter	Value		
Sweep #	1	2	3
$p$	2	3	4
$q$	0.01	0.1	1

**Table 2**  
Properties used for the simulation.

Property	Value	
Solid (316 stainless steel)	9960	988
Thermal conductivity [ $\text{W}/(\text{m} \cdot \text{K})$ ]	14.2	0.64
Specific heat [ $\text{J}/(\text{kg} \cdot \text{K})$ ]	465	4181
Dynamic viscosity [ $\text{Pa} \cdot \text{s}$ ]	-	$5.47 \cdot 10^{-4}$

design patterns of heat exchangers. The implementation of PPO with a CNN was facilitated using the Stable Baselines3 library for reinforcement learning [24]. This was complemented by the Gymnasium library, which provided a standardized framework for constructing and managing the simulation environment [25].

The state of the DRL algorithm is a 3D array with dimensions  $64 \times 128 \times 1$ . The first two dimensions represent the height and width information, and the last dimension represents the color information, where 0 represents black and 255 represents white. The action space is discrete, consisting of two possible actions: 0 and 1. Each action modifies the design of the heat exchanger, i.e., the solid- or fluid-like status of the nth cell, which changes the state of color information. The change in the temperature difference at the inlet and outlet obtained in the previous and current iterations was employed as the reward. The entire process was repeated until all 80 cells were simulated. To minimize the calculation time required for the thermofluidic finite element model (FEM) simulation, the algorithm loaded the data if they were calculated within the same heat exchanger shape; otherwise the FEM simulation was again conducted using COMSOL, and the data were saved for processing to prevent overlap. After a cycle, if the total reward represented the maximum value, which is the optimization goal, it was saved and was considered as the initial design.

Heat and fluid solvers were used for the simulation environment, and to reduce calculation time, the hot- and cold-fluid domains were assumed to be identical in design. The heat transfer between the plates was calculated using the same method of heat calculation used in the topology optimization method without the topology boundary described in Section 2.2. The inlet fluid temperatures of hot and cold were 80 and 20 °C, and the flow rate was 0.01 L/min on each plate.

Next, key hyperparameters were selected to optimize the heat exchange performance: the learning rate was set to 0.004, step size to 4096, and batch size to 256. The model was trained over ten epochs to ensure adequate learning without overfitting, and a discount factor of 0.99 was applied to slightly prioritize long-term rewards over immediate gains. The clip range was set at 0.2 to constrain policy updating and encourage stability, and the generalized advantage estimation was set to 0.95.

The initial design cell number was 80; however, obtaining results with a large mesh is difficult because of the extensive computational time required. Initially, 20 cells were employed for DRL to determine the number of episodes required to achieve a stable result. Subsequently, 80 cells were applied with that number of episodes to determine the maximum reward value. Fig. 5 presents a graph of the reward when 20 cells were considered, indicating that the maximum reward was achieved after 195 episodes. While focusing on maximizing the rewards, an 80-cell variant was simulated with 949 episodes, which was deemed sufficient to determine the optimal initial variables.

### 2.4. 3D printing manufacturing

The DRL-assisted topology-optimized heat exchanger was fabricated using additive manufacturing with a powder-based fusion 3D metal printer (AnyX-1000) to create a detailed flow path for the heat exchanger. The material used, SUS316L, is commonly employed in the industry owing to its excellent corrosion resistance, mechanical strength, and thermal resistance. The SUS316L powder size ranged

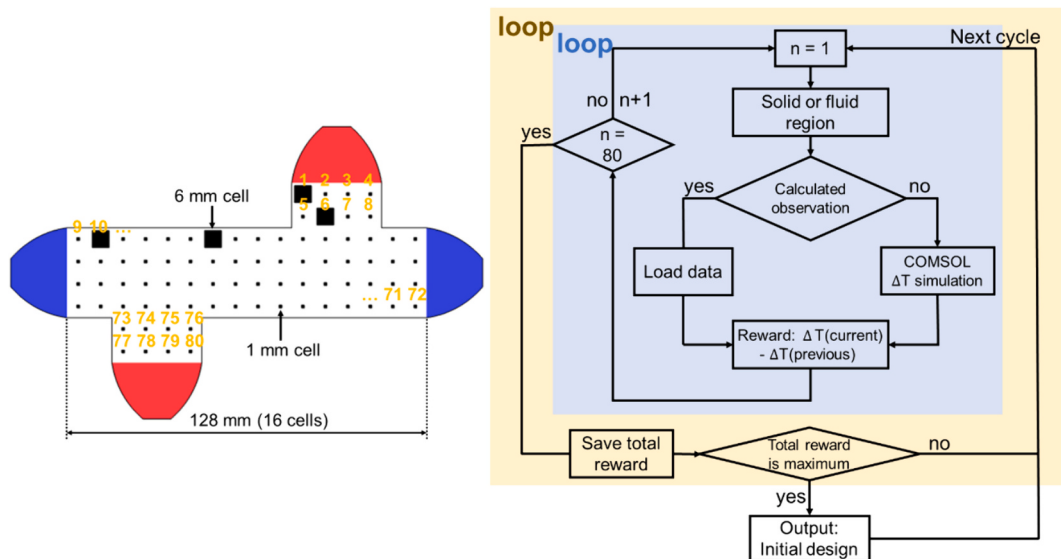


Fig. 4. Algorithm for DRL initial design.

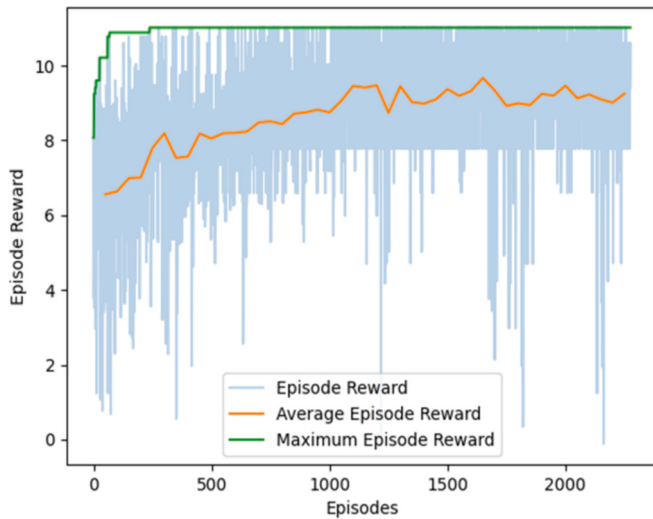


Fig. 5. Reward according to the episodes.

within 15–45  $\mu\text{m}$ . To facilitate additive manufacturing, the heat exchanger design was tilted at 45°, creating a rectangular flow path, and was divided into four caps and a heat exchanger body, as depicted in Fig. 6. Wire cutting was employed to detach the completed exchanger from the support. Finally, stainless-steel welding was used to merge the caps and heat exchanger; the completed device is shown in Fig. 7. A leakage test was performed with water flowing off each side.

## 2.5. Experiment and 3D simulation

An experimental loop comprising two constant-temperature water baths (T-101 and T-201), two pneumatic positional piston control valves (AV-101 and AV-201), four k-type temperature sensors (TE-101, TE-102, TE-201, and TE-202), and two magnetic inductive flow meters (FT-101 and FT-201) was constructed to verify the simulation results. The loop system diagram constructed with the IoT instrumentation of the specially designed mFinder-TAD is shown in Fig. 8. The flow rate was adjusted from 0 to 0.3 L/min using the valves, and the temperatures were measured to calculate the heat transfer capability of the heat exchanger. The flow meters measured the flow rates with a resolution of

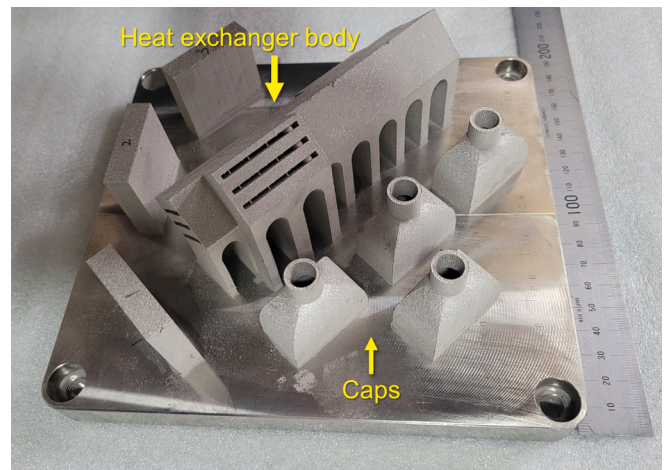


Fig. 6. Manufactured 3D printed heat exchanger components on their support.

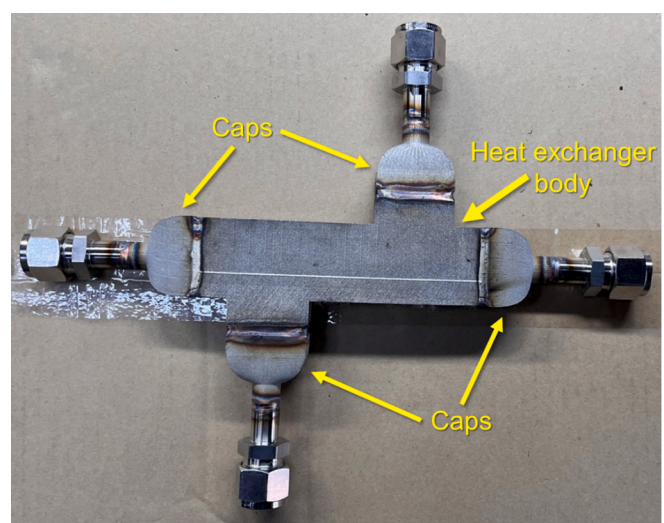


Fig. 7. Manufactured heat exchanger after assembly.

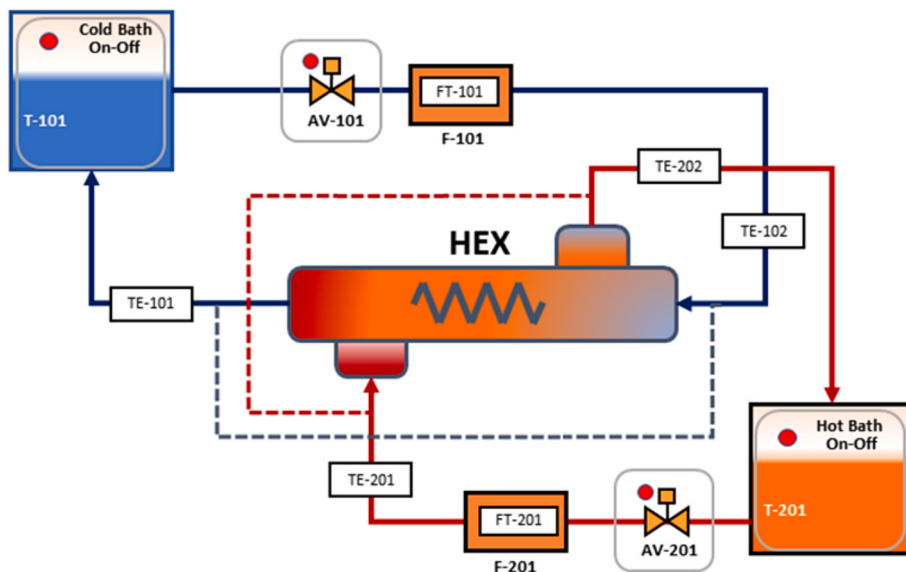


Fig. 8. Diagram of the experimental verification loop system.

0.00625 L/min. An image of the experimental loop system is provided in Fig. 9.

The overall uncertainty ( $\sigma_{\text{total}}$ ) was obtained as the root sum of the squares of all differences that contains systematic and random uncertainties, namely the temperature measurement uncertainty ( $\sigma_{t,m}$ ) of 0.75%, flowmeter measurement uncertainty ( $\sigma_{f,m}$ ) of 0.8%, flowmeter resolution uncertainty ( $\sigma_{f,r}$ ), and random uncertainty ( $\sigma_{t,r}$ ) of the temperature obtained by repeating the experiment seven times.

$$\sigma_{\text{total}} = \sqrt{\sum (\sigma_{t,m} + \sigma_{t,r})^2 + \sigma_{f,m}^2 + \sigma_{f,r}^2} \quad (8)$$

The 3D simulation was conducted with the governing equations expressed in Eqs. (1)–(3) without the shallow channel approximation and inverse permeability. The boundary condition of the inlet temperature of the cold and hot plates was changed as an experimental measured value to make the same condition of it.

A mesh grid sensitivity analysis, as presented in Table 3, was conducted. The M2 mesh elements, which have a 0.6% error compared to the M1 mesh, were used for simulations. Fig. 10 illustrates the mesh configuration, designed to accommodate the complex geometry of the flow path.

**Table 3**  
Mesh grid independence of DRL-assisted heat exchanger 3D simulation.

Elements number	Heat transfer rate [W]	Percentage error
M1: 79,405,164	124.9	-
M2: 66,591,511	124.2	0.6
M3: 59,005,002	126.0	0.84
M4: 15,138,739	126.4	1.19
M5: 4,889,908	127.4	1.95

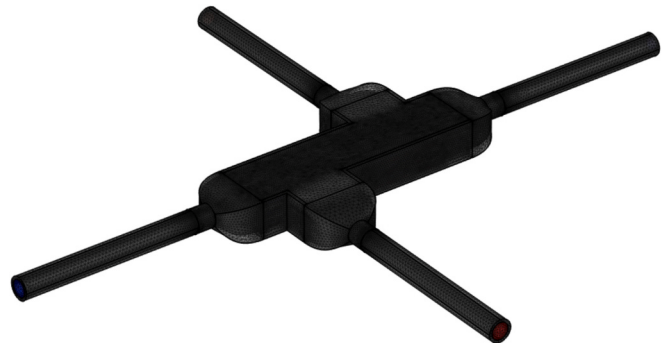


Fig. 10. Mesh structure for the 3D simulation.

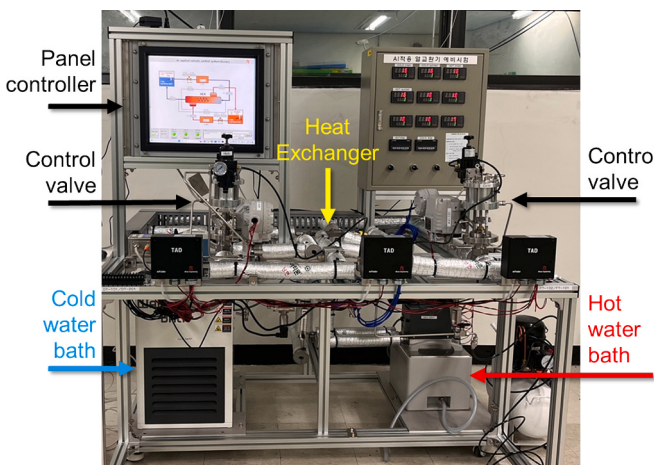


Fig. 9. Experimental loop system.

### 3. Results and discussion

The initial designs obtained via DRL using 800 episodes with a maximum reward were applied in the topology optimization process, as illustrated in Fig. 11. The topology-optimized heat exchanger designs obtained with and without the DRL-based initial design are shown on Fig. 11. These designs were subsequently compared, and the final topology-optimized designs were quite different.

The differences between the final 2D designs obtained by applying DRL to the initial design and conventional topology design are clear when considering the velocity distributions in Fig. 12, which illustrates why DRL is beneficial. The conventional topology optimization method produced a linear flow path, whereas the DRL-assisted topology optimization method produced a more twisted flow path that could reasonably maximize heat transfer for the designated pressure drop constraint.

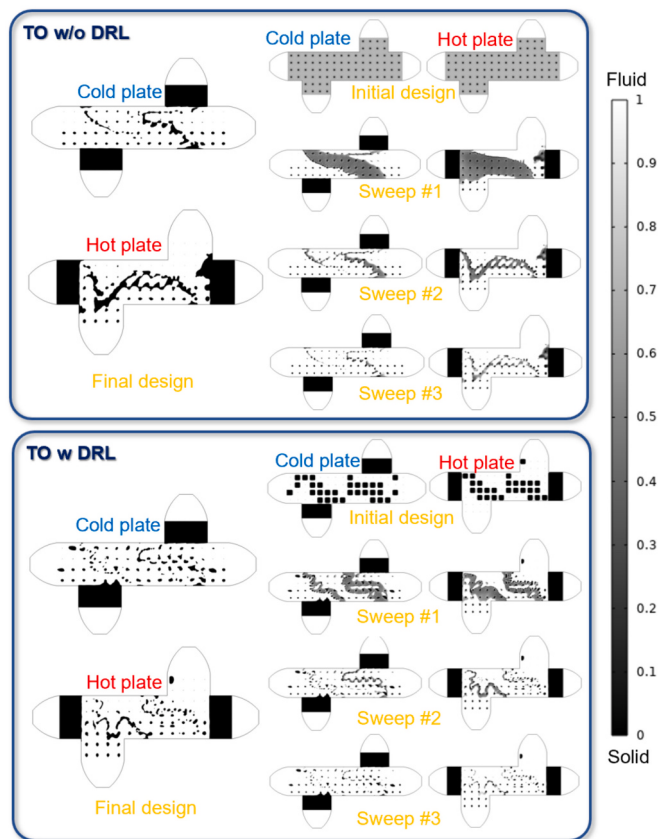


Fig. 11. Result of topology optimization (TO) with/without DRL.

Three-dimensional simulations of the original PCHE, conventional topology-optimized PCHE, and DRL-assisted topology-optimized PCHE were compared. Fig. 13 shows plots of the heat transfer rate according to the flow rate for each PCHE design. In the simulation, the flow channel of the original PCHE was configured with four channels, corresponding to the cell design size of the DRL heat exchanger as illustrated in Fig. 4. At a flow rate of 0.3 L/min, the heat transfer rates for the original design, conventionally optimized model, and DRL-assisted optimized PCHE were 423, 487, and 560 W, respectively, and the corresponding pressure drops were 54.3, 64.3, and 52.7 Pa, respectively. These results indicate that employing DRL-assisted topology optimization enhances heat

transfer efficiency, particularly under lower pressure differences. Notably, the heat transfer rate of the DRL-assisted topology-optimized PCHE design exceeded that of the original PCHE by 32.2% and surpassed the conventionally optimized PCHE by 14.8%.

Subsequently, an experiment was conducted on a 3D-printed PCHE reflecting the DRL-assisted topology-optimized design to confirm the simulated heat transfer rate according to flow rate. Table 4 shows the results of the experiment with mean and sigma values, and Fig. 14 shows the comparison between the experimentally obtained heat transfer rates and simulation values.

The experiment was performed seven times to adjust the flow rate until the temperature reached saturation. During the experiment, the control valve and other measurement devices were not insulated; therefore, the input value of hot and cold temperatures differed according to the flow rates. In the experiment, the temperature was measured near the end of the flow channel, as shown in Fig. 14. The difference between this measured value and the average value was then correlated to determine the heat transfer rate. A comparison between the correlated experimental and simulation heat transfer rates is presented in Fig. 15.

The 3D printed heat exchanger was cut via the wire cutting method to investigate the heat transfer rate differences shown in Fig. 16. The simulation considered flat surfaces with laminar flow. The heat transfer rate was lower than expected because of the following reasons:

- 1) The surface roughness of metal 3D-printed parts is typically higher than that of precision-machined parts. However, at lower Reynolds numbers, the presence of low-velocity fluid in the roughness valleys can decrease the heat transfer coefficient. Kadivar et al. [26] show that thermal performance is reduced at lower Reynolds numbers with low roughness. This observation may explain the differences observed in the results at low flow rates (0.06 to 0.18 L/min).
- 2) The heat exchanger was additively manufactured tilting by 45°, which generated unnecessary linear shapes of the flow channels. These impurity shapes could have interrupted the intended fluid flow.
- 3) Despite the welding between the caps and heat exchanger body shown in Fig. 7, the shape and material properties changed close to the welding area particularly in the surface parts.
- 4) The natural convection would have affected the heat exchanger surface despite it being insulated. This could have made the temperature difference larger at a lower flow rate on the hot plate side, which could have yielded a higher heat transfer rate in the experimental data.

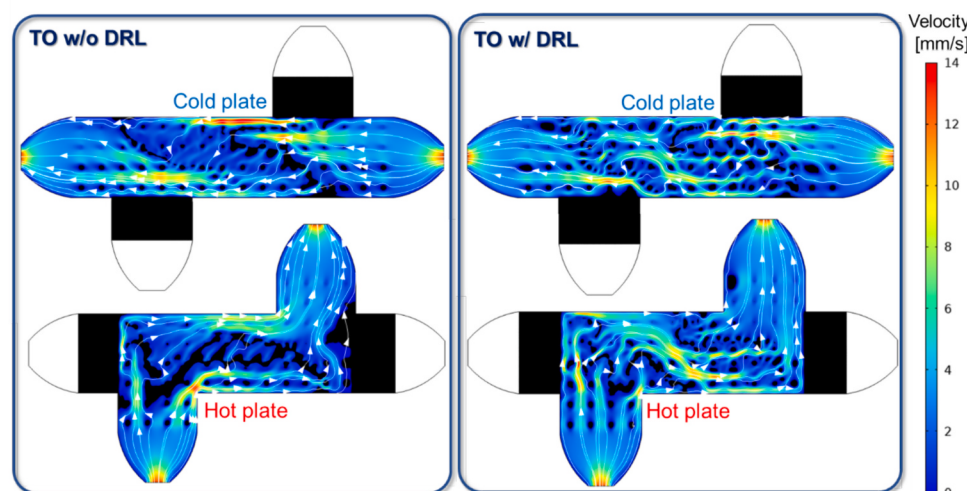


Fig. 12. Velocity distribution of topology-optimized heat exchanger designs with and without DRL-based initial design.

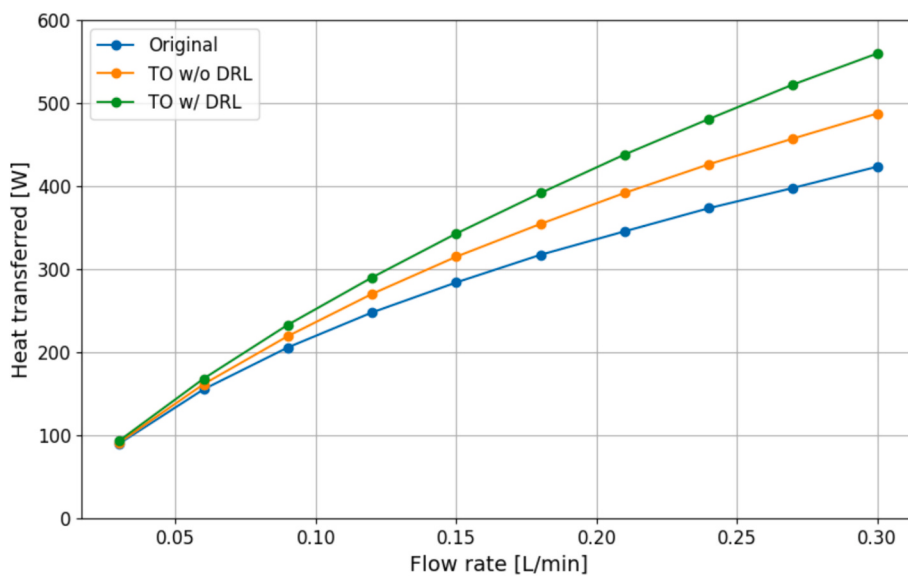


Fig. 13. Heat transfer rates according to flow rate for the three PCHE cases.

**Table 4**  
Experimental measurement results of temperatures according to the flow rate.

Flow rate [L/ min]	Hot inlet temperature [°C]	Hot outlet temperature [°C]	Cold inlet temperature [°C]	Cold outlet temperature [°C]
0.06	68.50±0.71	48.53±0.93	23.56±0.31	42.97±1.22
0.12	73.89±0.77	55.56±1.74	23.37±0.38	41.81±1.30
0.18	76.44±0.91	58.11±1.28	23.07±0.19	41.36±1.51
0.24	77.81±0.99	56.83±0.72	22.97±0.20	40.77±1.00
0.30	78.90±0.70	58.13±0.75	22.89±0.18	40.94±0.53

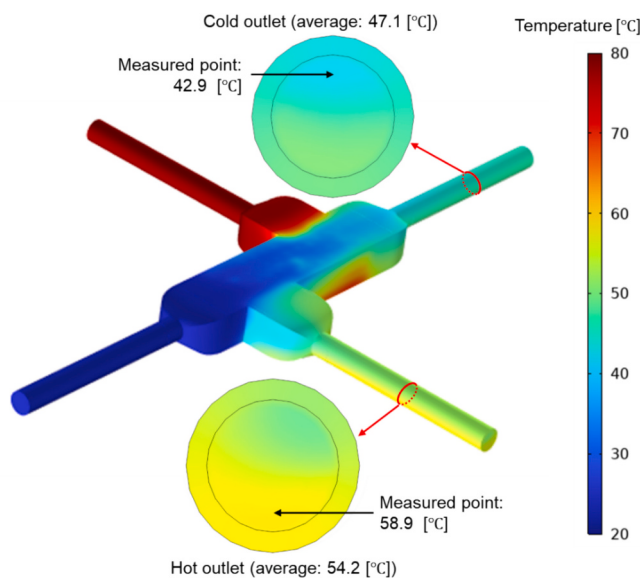


Fig. 14. Temperature distribution and measured points of the DRL-assisted heat exchanger at a flow rate of 0.3 L/min.

#### 4. Conclusion

This study introduced an innovative approach to thermofluidic dynamic topology optimization by employing DRL in the critical initial design phase. The DRL-assisted optimization method yielded significant

improvements in heat exchanger performance. Simulation results showed that the DRL-assisted optimized design achieved a 32.2% increase in heat exchange capability compared to the original PCHE design and a 14.8% improvement over a conventionally topology-optimized PCHE. These results clearly demonstrate the potential of DRL in enhancing heat exchanger efficiency. The practical performance verification of a complex heat exchanger manufactured using metal 3D printing further validated the feasibility of this technology. The performance is not completely aligned with the simulation results, so further research is needed to refine this technique and bridge the gap between simulation and practical implementation. This study demonstrated that DRL-assisted heat exchanger optimization can provide a novel approach to thermal system design, contributing to energy efficiency improvements that could be applicable to various industrial applications.

#### Funding

This study was supported by the Korea Atomic Energy Research Institute (KAERI) R&D Program [grant numbers KAERI-524490-23 and KAERI-524450-23].

#### Author contributions

G.L., Y.J., Y.Y., and H.K. planned and designed the research. G.L. and J.Y. led the topology optimization analysis. G.L. was in charge of developing the reinforcement learning models. S.L. created the heat exchanger using 3D printing techniques. T.K. designed and built the loop system to test the heat exchanger. G.L. and T.K. carried out experiments for the validation test. G.L. wrote the manuscript with input from Y.J., while Y.Y. and H.K. supervised and coordinated the overall research efforts.

#### CRedit authorship contribution statement

**Geunhyeong Lee:** Writing – original draft, Visualization, Validation, Software, Methodology, Investigation, Formal analysis, Data curation, Conceptualization. **Younghwan Joo:** Writing – review & editing, Supervision. **Sung-Uk Lee:** Validation. **Taejoon Kim:** Validation, Data curation. **Yonggyun Yu:** Supervision, Funding acquisition. **Hyun-Gil Kim:** Supervision, Funding acquisition.

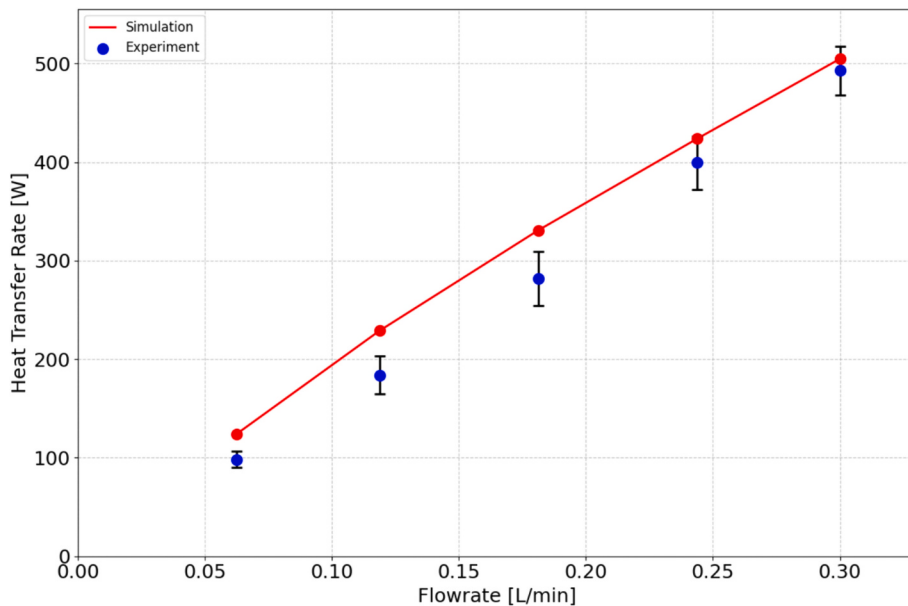


**Fig. 15.** Experimentally obtained heat transfer rate according to flow rate.

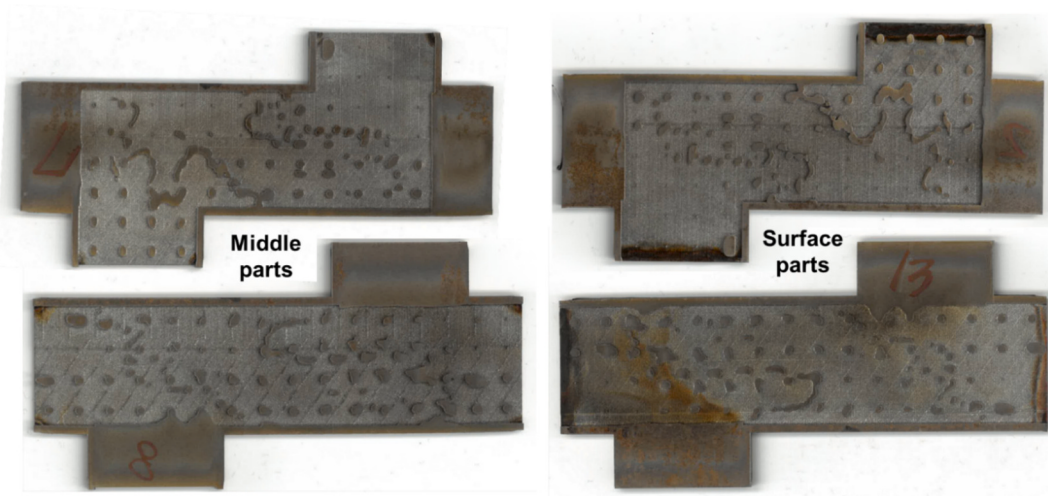


**Fig. 16.** 3D printed heat exchanger flow channels through the wire cutting.

#### Declaration of competing interest

The authors declare no competing interests.

#### Data availability

Data will be made available on request.

#### References

- [1] T. Ma, M.-J. Li, J.-L. Xu, F. Cao, Thermodynamic analysis and performance prediction on dynamic response characteristic of PCHE in 1000 MW S-CO<sub>2</sub> coal fired power plant, *Energy* 175 (2019) 123–138.
- [2] A. Di Ronco, A. Cammi, S. Lorenzi, Preliminary analysis and design of the heat exchangers for the Molten Salt Fast Reactor, *Nucl. Eng. Technol.* 52 (1) (2020) 51–58.
- [3] C.W. Shin, Experimental study for pressure drop and flow instability of two-phase flow in the PCHE-type steam generator for SMRs, *Nucl. Eng. Des.* 318 (2017) 109–118.
- [4] S.W. Lee, S.M. Shin, S. Chung, H. Jo, Evaluation of thermal-hydraulic performance and economics of printed circuit heat exchanger (PCHE) for recuperators of Sodium-cooled Fast Reactors (SFRs) using CO<sub>2</sub> and N<sub>2</sub> as working fluids, *Nucl. Eng. Technol.* 54 (5) (2022) 1874–1889.
- [5] K.-Q. Chen, W.-H. Pu, Q. Zhang, B.-S. Lan, Z.-Y. Song, Y.-Q. Mao, Thermal performance analysis on steady-state and dynamic response characteristic in solar tower power plant based on supercritical carbon dioxide Brayton cycle, *Energy Sources Part A* (2020) 1–23.
- [6] M. Saeed, A.S. Berrouk, M. Salman Siddiqui, A. Ali Awais, Effect of printed circuit heat exchanger's different designs on the performance of supercritical carbon dioxide Brayton cycle, *Appl. Therm. Eng.* 179 (2020) 115758.
- [7] Y. Yang, H. Li, B. Xie, L. Zhang, Y. Zhang, Experimental study of the flow and heat transfer performance of a PCHE with rhombic fin channels, *Energy Convers. Manag.* 254 (2022) 115137.
- [8] P. Papazoglou, Topology optimization of heat exchangers, Master's thesis, Delft University of Technology, 2015.
- [9] K.R. Saviers, R. Ranjan, R. Mahmoudi, Design and validation of topology optimized heat exchangers, in: A.I.A.A. Scitech (Ed.), Forum. Presented at the AIAA Scitech 2019 Forum, American Institute of Aeronautics and Astronautics, San Diego, California, 2019.
- [10] L.C. Høghøj, D.R. Nørhave, J. Alexander, O. Sigmund, C.S. Andreassen, Topology optimization of two fluid heat exchangers, *Int. J. Heat Mass Transf.* 163 (2020) 120543.
- [11] F. Feppon, Shape and topology optimization applied to compact heat exchangers, *HAL Open Sci. hal-03207863* (2021) 2021.
- [12] F. Feppon, G. Allaire, C. Dapogny, P. Jolivet, Body-fitted topology optimization of 2D and 3D fluid-to-fluid heat exchangers, *Comput. Methods Appl. Mech. Eng.* 376 (2021) 113638.

- [13] G. Lee, Y. Joo, Y. Yu, H.-G. Kim, Dual-fluid topology optimization of printed-circuit heat exchanger with low-pumping-power design, *Case Stud. Therm. Eng.* 49 (2023) 103318.
- [14] J. Gao, H. Li, Z. Luo, L. Gao, P. Li, Topology optimization of micro-structured materials featured with the specific mechanical properties, *Int. J. Comp. Methods* 17 (3) (2020) 1850144.
- [15] S. Shin, D. Shin, N. Kang, Topology optimization via machine learning and deep learning: a review, *J. Comp. Design Eng.* 10 (4) (2023) 1736–1766.
- [16] S. Jang, S. Yoo, N. Kang, Generative design by reinforcement learning: Enhancing the diversity of topology optimization designs, *Comput. Aided Des.* 146 (2022) 103225.
- [17] B.S. Mekki, J. Langer, S. Lynch, Genetic algorithm based topology optimization of heat exchanger fins used in aerospace applications, *Int. J. Heat Mass Transf.* 170 (2021) 121002.
- [18] J. Schulman, F. Wolski, P. Dhariwal, A. Radford, O. Klimov, *Proximal Policy Optimization Algorithms*, 2017.
- [19] J.H.K. Haertel, K. Engelbrecht, B.S. Lazarov, O. Sigmund, Topology optimization of a pseudo 3D thermofluid heat sink model, *Int. J. Heat Mass Transf.* 121 (2018) 1073–1088.
- [20] COMSOL AB, *CFD Module User's Guide*. COMSOL Multiphysics® v. 6.0, Stockholm, Sweden, 2021.
- [21] COMSOL AB, *Optimization Module User's Guide*. COMSOL Multiphysics® v. 6.0, Stockholm, Sweden, 2021.
- [22] K. Svahnberg, MMA and GCMMA – Two Methods for Nonlinear Optimization, Technical Report, 2007.
- [23] Y. Cao, S. Li, L. Petzold, Adjoint sensitivity analysis for differential-algebraic equations: Algorithms and software, *J. Comput. Appl. Math.* 149 (1) (2002) 171–191.
- [24] A. Raffin, A. Hill, A. Gleave, A. Kanervisto, M. Ernestus, N. Dormann, Stable-baselines3: Reliable reinforcement learning implementations, *J. Mach. Learn. Res.* 22 (2021) 1–8.
- [25] G. Brockman, V. Cheung, L. Pettersson, J. Schneider, J. Schulman, J. Tang, W. Zaremba, OpenAI Gym, 2016.
- [26] M. Kadivar, D. Tormey, G. McGranaghan, CFD of roughness effects on laminar heat transfer applied to additive manufactured minichannels, *Heat Mass Transf.* (2022).